Experimental investigation of pipes with flexible joints under fault rupture

Vasileios E. Melissianos*
School of Civil Engineering – Institute of Steel Structures
National Technical University of Athens
9, Iroon Polytechneiou str.
Zografou Campus
GR-15780, Athens, Greece
email: melissia@mail.ntua.gr
tel: +302107722553

Xenofon A. Lignos
School of Civil Engineering – Institute of Steel Structures
National Technical University of Athens
9, Iroon Polytechneiou str.
Zografou Campus
GR-15780, Athens, Greece
email: lignosx@central.ntua.gr
tel: +302107722305

Konstantinos K. Bachas
School of Civil Engineering – Institute of Steel Structures
National Technical University of Athens
9, Iroon Polytechneiou str.
Zografou Campus
GR-15780, Athens, Greece
email: kbachas@hotmail.com

Charis J. Gantes
School of Civil Engineering – Institute of Steel Structures
National Technical University of Athens
9, Iroon Polytechneiou str.
Zografou Campus
GR-15780, Athens, Greece
email: chgantes@central.ntua.gr
tel: +302107723440

*Corresponding author additional contact: melissianosv@gmail.com

KEYWORDS: experimental tests, buried pipes, flexible joints, fault rupture, numerical analysis

ABSTRACT

Objective of the present study is the experimental investigation and comparison of the response of continuous pipes and pipes with internal flexible joints under imposed transverse displacement, modeling seismic fault rupture. Three-point bending tests were performed modeling the deformation of buried pipes subjected to fault offset. The introduction of flexible joints between adjacent pipeline parts is proposed as an alternative protection measure to reduce developing strains due to such offsets. Indeed, experimental results confirmed very significant contribution of flexible joints in strain reduction, thus providing strong promise of effective protection of buried pipes from the principal failure modes occurring in such cases, i.e. local buckling of pipe wall and tensile fracture of girth welds between adjacent pipeline segments. Experimental results have been sufficiently reproduced by numerical simulation accounting for geometric and material nonlinearities and incorporating longitudinal residual stresses due to seam weld. The numerical analyses and corresponding results are also presented in detail.

1. Introduction

Onshore buried steel fuel pipelines extend over long distances and when seismic areas are traversed, crossing tectonic faults might be inevitable. Fault offset is considered to be the major cause of pipeline failure due to seismically induced actions [1]. Due to the hazardous nature of pipelines, there is an ongoing effort to propose effective measures for their protection against the consequences of faulting. Pertinent efforts focus on reducing the risk of local buckling of pipe wall and tensile fracture of girth welds, which are the two principal failure modes in such case. Various mitigating measures have been implemented by the industry, such as pipe wall thickness increase, steel grade upgrade and pipe wrapping with geotextiles in order to reduce pipe-soil friction [2], embedding the pipeline in soft soil, choosing appropriate angle of fault crossing, introducing bends (e.g. elbows) at some distance from the fault zone to enhance flexibility, etc.

The present work is part of a feasibility study of a new mitigating measure, namely introducing flexible joints between adjacent pipe parts, following the ideas of Bekki et al. [3]. The aim is to concentrate the developing strains at the joints and retain the pipe steel parts virtually undeformed and consequently unstressed [4]. Flexible joints are used in industrial piping networks to absorb thermal expansion, thrust and machinery vibration.

Strength and deformation capacity of pipes has been experimentally investigated for over five decades. The mechanical behavior of buried pipes subjected to permanent ground displacements (PGDs) is a complex pipe – soil interaction problem, given that the pipe is forced to follow the PGDs by developing extensive deformation. Thus, when the surrounding soil is incorporated in an experimental investigation, numerous constructional, cost and time consuming issues emerge. The experimental investigation of pipes can therefore be roughly divided into two main categories: (i) Pipes without surrounding soil. The tests are usually three- or four-point bending tests with simple boundary conditions (e.g. cantilever, clamped beam, etc.) and simple or combined external loading (e.g. bending, axial force, internal pressure). The major objective of these experiments is the estimation of pipe bending capacity, pre- and post-buckling behavior and critical compressive buckling strain. (ii) Pipes with surrounding soil, where the experimental set-up is usually a shear-box or a centrifuge, used to assess the behavior of a pipe subjected to faulting, soil liquefaction or settlement by considering the effect of various relevant parameters (e.g. soil characteristics, pipe diameters and thickness, burial depth, etc.).

Literature on the topic of experimental investigation of pipes without surrounding soil is broad. Experimental studies on the strength and deformation capacity of tubes and pipes have been presented in [5], [6], [7], [8]. In the middle of the 1980's, Gresnigt [9] published the results of an extensive experimental study of pipes in a prominent textbook, focusing on the plastic design of pipes subjected to permanent ground displacements. Then, important experimental studies have been also presented by Yoosef-Ghodsi et al. [10], Murray [11] and Gresnigt et al. [12], [13]. Recently, Dame et al. [14] performed full-scale four-point bending tests of API5L Grade B pipes with external diameter of 24in to study the structural behavior of pipes under bending and internal pressure. Thinvongpituk et al. [15] experimentally investigated steel pipes with diameter over thickness (D / t) ratio ranging from 21.16 to 42.57 under pure bending to validate a proposed analytical methodology for the estimation of pipe cross-section ovalization. Then, Gresnigt and Karamanos [16] presented a study on previous experimental results, focusing on the elastoplastic local buckling of pipes and the effect of the manufacturing process on the pipe ultimate capacity and local buckling. Mason et al. [17] were the first to perform tensile tests of full-scale API5L Grade B pipes with welded slip joints (WSJ) to investigate the strength of joints. Chen et al. [18] performed full-scale experiments of 40in diameter X70 pipes under bending, compression and internal pressure to assess their strength. Later, Ferino et al. [19] carried out experiments on full-scale X80 pipes (D/t ratio from 50 to 65) to examine the critical buckling strain of high-strength steel pipes. Recently, Kristoffersen et al. [20] presented experimental results from three-point bending tests of in-scale offshore X65 pressurized pipelines under transverse and axial forces and internal pressure to investigate the relationship between axial load, bending capacity and cross-sectional distortion. Experimental results have been used to formulate the provisions of pertinent codes and standards regarding the strength and deformation capacity of onshore and offshore pipes, e.g. API [21], ASME [22], [23], CSA [24], [25], DNV [26].

Experimental tests of buried pipes with surrounding soil are quite limited in the literature. Abdoun et al. [27] used a centrifuge to investigate in-scale HDPE pipes subjected to strike-slip faulting focusing on the fault offset rate, the backfill soil moisture content, the burial depth and the pipe diameter. A year later, Ha et al. [28] used the same centrifuge to experimental investigate HDPE pipes in order to compare the obtained results to those reported after the failure of a major water pipeline in Izmir (Turkey), caused by the 1999 Kocaeli earthquake [29]. A major finding was that the locations where local buckling occurred, acted as “flexible joints” in case of increasing fault offset. Then, Rofooei et al. [30] utilized a shear box in order to rigorously model the response of an API5L Grade B pipe with 4in diameter subjected to reverse faulting. The reverse faulting caused inelastic pipe local buckling both in the fault footwall and hanging wall part. Moradi et al. [31] used a centrifuge to investigate the behavior of stainless steel pipes under normal faulting, considering the relationship between axial and bending strains and the effects of burial depth and fault offset magnitude. Very recently, in the final report of the RFCS project GIPIPE [32], results of small-scale experiments of pipes under faulting (normal of reverse) using a shear box were presented and were used to calibrate numerical models. Additionally, in the same study, axial pulling tests were performed in order to evaluate the developing pipe – soil friction and full-scale tests were executed, simulating the imposed ground displacement due to landslide or faulting. Experimentally obtained pipe strains were compared to code-based predictions and the locations of strain concentrations were investigated.

Experimental investigation on the efficiency of alternative mitigating measures against the consequences of faulting on pipelines is however quite limited until now. Hedge et al. [33] tested small diameter PVC pipes embedded in geocell reinforced sand beds in order to investigate the efficiency of geocells in terms of protecting buried pipelines. The experimental set-up consisted of a test tank filled with sand, where the pipeline was placed at the bottom, while force was applied on the top soil surface through a hydraulic jack. Sim et al. [34] performed shaking table tests of small diameter pipes crossing a vertical fault to investigate the performance of tyre derived aggregate (TDA) backfill in terms of protecting buried pipelines against vertical faulting and shaking. The obtained experimental results showed that TDA backfill contributes to pipe bending moment reduction. Monroy-Concha [35] carried out tests of pulling pipes embedded in sand backfill so as to examine the effect of covering trench's walls with geotextiles on the buried pipe protection. Finally, experimental investigation of flexible joints as individual components, i.e. without considering them as part of a piping network, have been primarily conducted to determine the mechanical properties of the joint [36], [37].

Seismic fault activation is associated to PGDs and thus the problem under investigation is displacement-controlled and consequently strain-controlled rather than stress-controlled. Extensive yielding is expected to take place due to faulting, while the corresponding strains might remain below a limit that is associated to failure, i.e. concentration of tensile strains is associated with tensile rupture at girth welds, while compressive strains with local buckling of the pipeline wall. Pertinent structural codes for the design of buried pipes at fault crossings provide strain-limit expressions for both compressive and tensile strains (e.g. [38],[39]).

The objective of the experimental investigation presented here was to study the efficiency of flexible joints integrated in tubes under transverse imposed displacement, modeling fault movement, in terms of reducing longitudinal strains and consequently preventing tube failure. Unpressurized continuous tubes and a tube with internal flexible joints were tested and the obtained results were compared to identify the repercussions of joints in the overall tube response, while special focus was paid on comparing the developing strains in light of the pipeline strain-based design rules. Then, the experimental results were compared to corresponding numerical ones, obtained from nonlinear analyses of finite element models. Details of both the tests and their numerical modeling are presented in the following sections.

It must be noted that this application of flexible joints has not been so far used in practice. In the present study some aspects of the joints' efficiency in protecting buried pipes from fault activation are investigated. However, considerable constructional and practical issues have to be tackled in addition, before practical application can actually be implemented, which are beyond the scope of this paper. Such issues include bellow protection against corrosion, pipe – bellow proper welding, bellow isolation from the surrounding soil and bellow long-term behavior, response of buried pipelines under very high pressure or being surrounded with low friction soil, etc.

2. Description of experiments and experimental set-up

2.1 Specimens

A total number of four tubes have been tested at the Institute of Steel Structures in the School of Civil Engineering of the National Technical University of Athens. Fixed end conditions were selected at both specimens' ends aiming at proper modeling of the pipeline deformation due to faulting. Namely, the deformation of a buried pipeline subjected to strike-slip fault rupture is a smooth s-shaped curved line (Figure 1), where two anchor points represent the pipeline locations beyond which the structure is assumed to be unstressed. In the experimental set-up, the tubes were fixed at the ends, while the displacement was imposed in the middle-span. Thus, the deformation of each half of the specimen was expected to model the s-shaped deformation of a pipe (Figure 2), considering the fixed ends and the middle-span location as virtual anchor points.

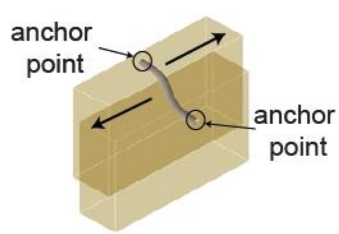

Figure 1: Schematic illustration of pipeline deformation subjected to strike-slip fault offset

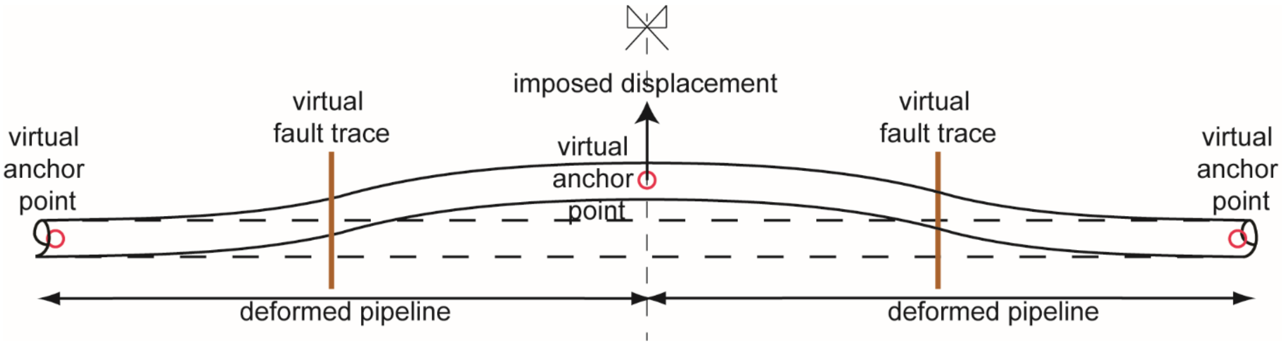

Figure 2: Schematic illustration of the experimental concept

Three continuous specimens were tested (N=1, N=2 and N=3), abbreviated as CP and one specimen with flexible joints (N=4), abbreviated as PFJ. Indicative sketches of the continuous specimens and the specimen with flexible joints are provided in Figure 3. The tubes were of cross-section CHS 114.3x3, selected on the basis of the geometrical restrictions of the testing frame, in order to have a realistic length over diameter ratio for each s-shaped deformed configuration. The length of the specimens was defined by the available length of the testing frame, and the fixed end conditions impose the locations of virtual anchor points, while in practice the location of the anchor points depends on the pipe – soil friction [32]. Additionally, the diameter over thickness ratio (*D*/*t*) of the CHS 114.3x3 cross-section is equal to 38.1, which was considered to be relatively low and in combination with the imposed displacement magnitude no local buckling was expected to occur in the elastic range.

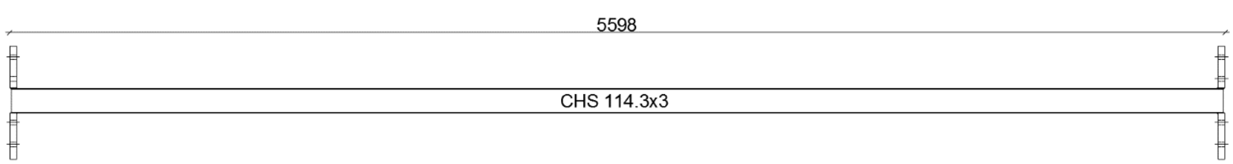

(a)

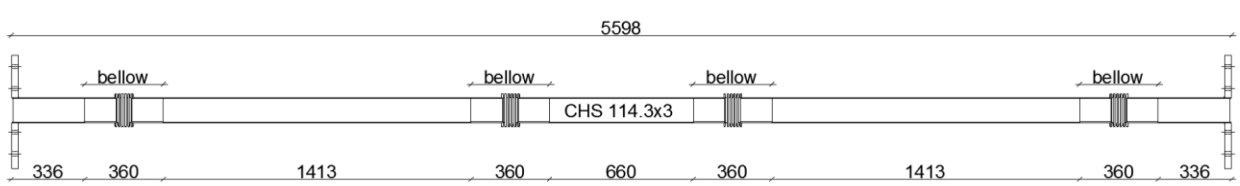

(b)

Figure 3: Specimen types: (a) CP and (b) PFJ

The structural system of the specimens was that of a beam with fixed ends, subjected to imposed displacement in the middle. The maximum bending moment was thus expected at the fixed ends and the middle. The introduction of flexible joints aimed at reducing the developing strains and thus their location was selected as close as possible to the maximum moments' locations, based on preliminary numerical analysis results and the restrictions of the measuring instruments. For the sake of completeness and with reference to buried pipes, it is noted that the uncertainty regarding the exact location of the fault trace has not been addressed by the testing process. This assumption does not affect the research objective of this study, which is to gain confidence regarding the effectiveness of bellow-type flexible joints in terms of reducing the pipe developing strains. The issue of uncertainty of fault trace and its effect on joint efficiency has been treated by the authors numerically, employing the numerical models validated by the presented experiments [40].

The maximum imposed displacement by the actuator was equal to one specimen diameter, i.e. about 115 mm, which was shown from preliminary numerical results to cause yielding of continuous specimens and was then chosen as the same for the specimen with flexible joints for reasons of comparison, considering also practical limitations due to the experimental set-up. Even though in actual cases of fault rupture the displacements may well exceed one pipeline diameter, numerical investigations of the authors [40] including rupture amplitudes up to four pipeline diameters have demonstrated that pipe parts remain elastic and imposed deformations are absorbed by rotations at the joints, which are within the elastic range of commercially available bellows. Regarding the latter issue, the behavior of bellows and the evaluation of their risk for rupture has been addressed by the axial and rotational tests of individual bellows (section 4), which were tested up to failure, exhibiting their capacity to sustain much larger deformations than encountered in the specimen with flexible joints subjected to displacement of one diameter.

2.2 Testing frame

The experimental set-up was the same for all four specimens. Indicatively, the PFJ specimen positioned in the testing frame is depicted in Figure 4. The specimens were connected to 30 mm thick endplates with tube socket joint fillet welds. Then, endplates were bolted to the testing frame with eight M20 8.8 bolts. The design of the specimen – testing frame connection was found to be sufficient for the expected magnitude and deflection of the connection to prevent yielding and to ensure that the connection would be sufficiently rigid. The specimen installation in the testing frame was carried out in two steps: (i) the bolts on one side were pretensioned, (ii) on the other side shim plates were inserted between the endplate and the frame column flange to fill any potential gap, and then the bolts were pretensioned. Developing strains on the specimen during bolt pretensioning were measured by strain gauges and the recorded strains were found to be very low compared to those recorded during the experiments, thus they were not considered thereafter. The displacement was imposed through a flange (referred thereinafter as loading flange) that was connected to the actuator via a wire rope. The loading flange was designed to be sufficiently thick (40 mm) to ensure uniform load application on the specimen and consequently avoid any undesirable local failure of the tube. Hence, the structural system of the PFJ specimen was that of a beam with fixed ends and four internal flexible hinges. Thus, temporary support was necessary before the test to avoid sagging.

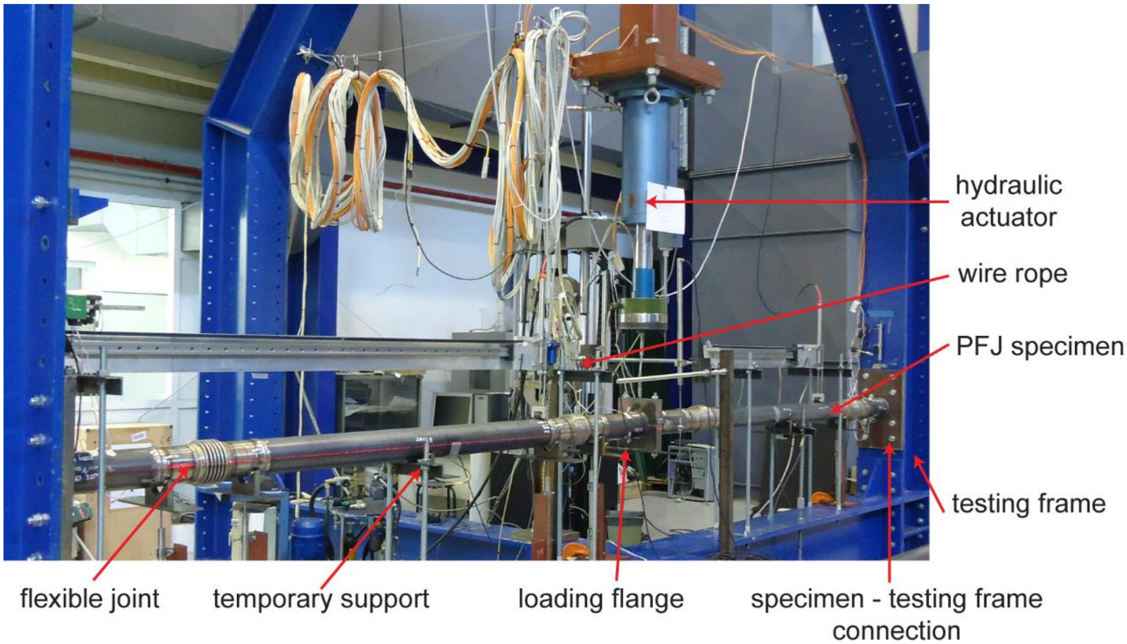

Figure 4: View of PFJ specimen at the testing frame

2.3 Testing procedure and measuring devices

The tests were performed using a 300 kN hydraulic actuator of maximum pressure equal to 125 bar, operating in displacement control. The rate of the imposed displacement was in all cases equal to 0.032 mm/s. The reaction force was measured by a load-cell mounted at the actuator's head. The measuring devices' configuration was nominally identical in all specimens and it is indicatively illustrated in Figure 5 for specimen N=4.

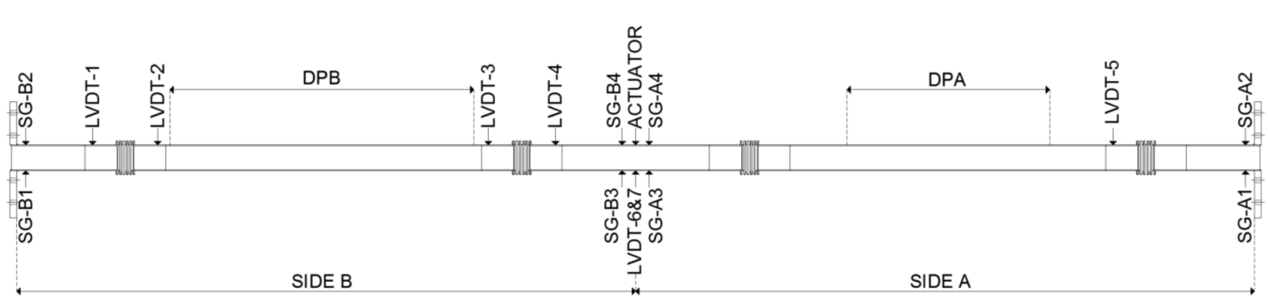

Figure 5: Configuration of measuring devices

Individual Linear Variable Differential Transformers (LVDTs) were installed to measure the specimen's deflection (vertical displacement in-plane with imposed displacement) at bellow edges (Figure 6), in order to identify the differences between the CP and PFJ deformation. Two additional

LVDTs were installed on the loading flange (ACTUATOR) to monitor the true specimen displacement, since the displacement recorded by the load-cell could be affected by the electromagnetic noise of the actuator operation, the wire rope expansion and other relevant parameters.

Furthermore, a 2D Deformation Plotter (DP) was designed and constructed in the Institute of Steel Structures NTUA in order to plot the specimen's deformed shape (Figure 8). The main transducers of DP were a LVDT monitoring the vertical displacement and a wire-type displacement transducer, monitoring the longitudinal coordinate. Thus, DP was capable of scanning the specimen's deformation, i.e. monitoring simultaneously the vertical and the longitudinal coordinate at predefined time steps. The LVDT was attached to the movable part of the system, namely the linear table, which was sliding along an aluminum linear guide. Motion of the system was provided by an electric stepper motion and was transmitted via a timing belt. Then, in order to provide uninterrupted sliding of the LVDT's rod on the specimen's surface, an appropriately constructed roller system was mounted on the LVDT's rod edge. The system (DP) was assembled on a thick aluminum base, which was installed on supporters at a sufficient distance above the specimen, determined by the maximum LVDT stroke and the maximum expected vertical displacement of the specimen. The system was controlled by an in-house built computer-driver, controlling the micro-steps of the stepper motor rotation (each full rotation of the motor consisted of 200 steps and every step of 128 micro-steps), the velocity and the acceleration. Two DPs were constructed with maximum longitudinal plotting length capacity equal to 920 mm (DPA) and 1920 mm (DPB), respectively, and they were installed at the two sides of each specimen, left and right of the loading flange.

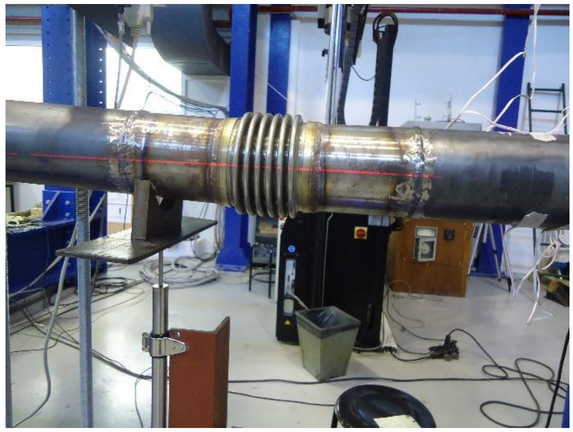

Figure 6: LVDT placed on a bellow's edge

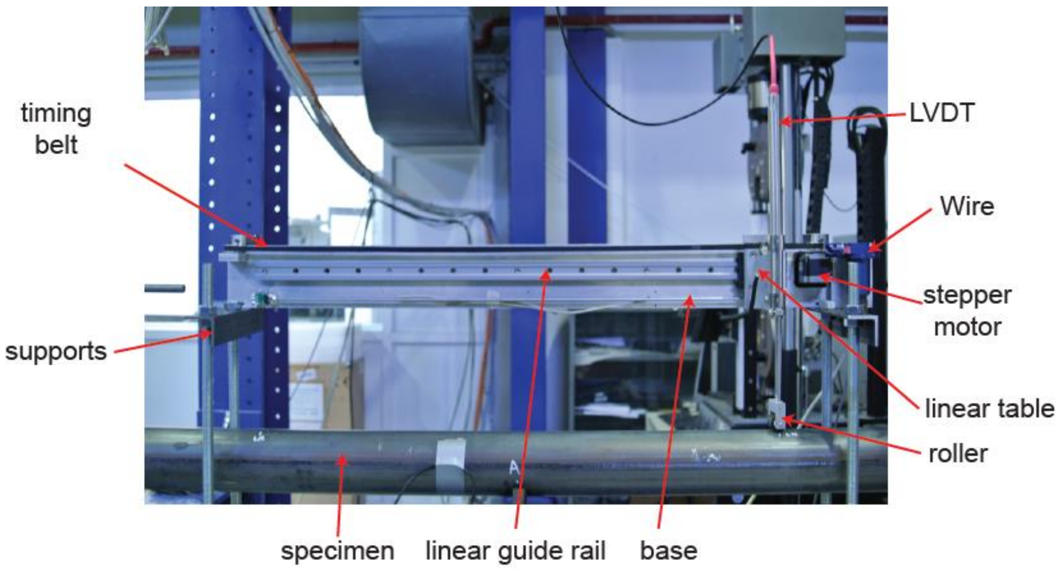

Figure 7: Parts of Deformation Plotter

Strains were measured with strain gauges (nominal resistance 120 Ω) that were placed at locations detailed in Figure 5 to measure the longitudinal tensile and compressive strains. The locations of strain gauges (SGs) were selected based on the maximum expected stress-state (Figure 8), which entered into plasticity. Special care was given for the correct placement of the strain gauges by polishing the desirable locations in order to ensure a satisfactory contact between the strain gauge and the specimen surface.

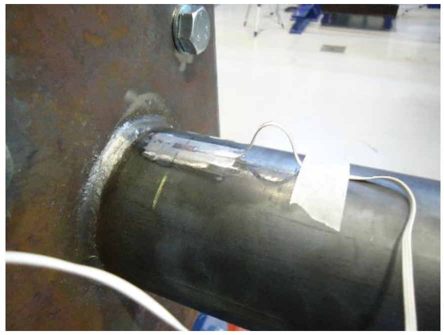

Figure 8: Strain gauge placed on tube crown

3. Steel properties

Tensile tests were carried out to extract the material properties of the steel used for manufacturing of the specimens. Appropriately design coupons cut from specimens during their construction were subjected to displacement-controlled tests. The geometry of the coupons and the testing procedure were based on the guidance provided by EN ISO 6892-1:2009 [41]. The tensile test results were provided in terms of the applied load and the corresponding displacement of the coupon's edges, from which the engineering stress (σ_e) and engineering strain (ε_e) could be calculated based on the coupons cross-section area. Then, in order to take into account the change of coupon's width during the loading process, the true stress (σ_t) and true strain (ε_t) were calculated according to the expressions:

$$\sigma_t = \sigma_e(1+\varepsilon_e) \quad (1)$$

$$\varepsilon_t = \ln(1+\varepsilon_e) \quad (2)$$

A view of a typical coupon at its final shape before testing is illustrated in Figure 9 and during testing in Figure 10. From each specimen (N=1 to N=4) three coupons where cut, named for example N=1.1 to N=1.3 for specimen N=1. An INSTRON 300 kN tensile testing machine was used and the elongation of the tensile test coupon was measured by an extensiometer mounted on the coupons over a gauge length of 50 mm.

Figure 9: Typical tensile coupon

Figure 10: Coupon during tensile test

The average modulus of elasticity for all specimens was found equal to 210 GPa, which is in accordance with the value provided in pertinent structural textbooks for steel. The yield stress for each coupon was taken as the 0.2% proof stress found in the plateau following the elastic branch. Typical true stress – strain curves obtained for tensile specimen N=2 are given in Figure 11a and a detail of the true stress – strain curves in Figure 11b to show the plateau and the strain hardening initiation. The mean true yield stresses for each specimen are listed in Table 2.

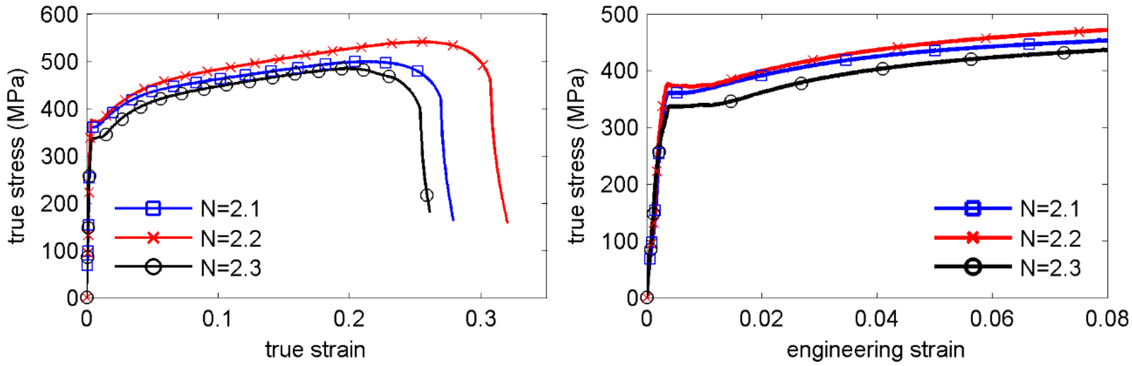

(a) (b)

Figure 11: (a) True stress – strain curves and (b) detail of the true stress – strain curves for steel of specimen N=2

Table 2: Mean yield stresses of specimens

	N=1	N=2	N=3	N=4
Yield stress (MPa)	355	354	344	345

4. Flexible joint properties

The flexible joints used in the present study were commercial metallic single bellows. The joint and its geometry are depicted in Figure 12. The material of the convolutions was stainless steel AISI 321L, while the pipe edges were made of carbon steel ST 37-2 to ensure proper connection through full-penetration butt welds with the carbon steel segments of specimen N=4.

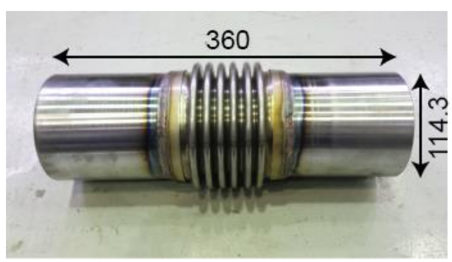

Figure 12: Flexible joint used in the experimental investigation

The bellow is designed to withstand pressure thrust, internal pressure and variations in the fluid temperature. The single bellow can accommodate elongation and shortening, lateral movement and rotation (Figure 13). The flexible joint type was selected based on its availability in the market and in light that the internal pressure was not considered in the investigation.

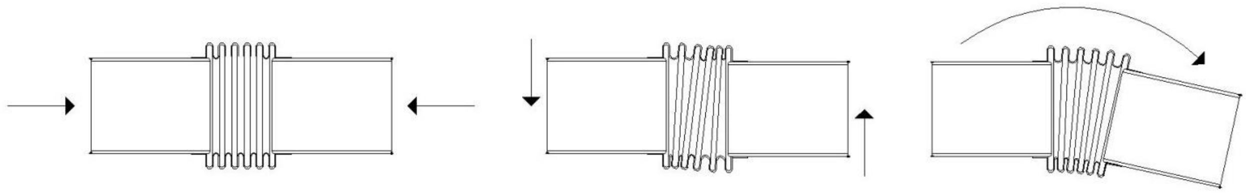

(a) (b) (c)

Figure 13: Definition of flexible joint's (a) axial, (b) lateral and (c) angular movement capability

The purpose of the presented experimental investigation was to quantify the contribution of flexible joints in strain reduction when integrated in pipes subjected to imposed displacement. It was thus necessary to measure their axial, lateral and angular stiffness. For that purpose, two individual experiments were performed to investigate the axial and the angular stiffness of the joint, respectively. It is noted that due to the inherent difficulty to experimentally decouple shear and bending, an individual experimental for measuring lateral stiffness was not carried out. This lack of data was decided to be handled using joint properties published on data sheets by joints manufactures. Commercial joint specifications indicate that for similar low pressure single joints, the ratio of axial over lateral stiffness can range from 0.25 to 0.75.

Firstly, an experiment was conducted to investigate the axial stiffness of the joint. The experimental set-up and the measuring devices are shown in Figure 14. The joint was welded between two CHS 114.3x3 segments, while two flanges were welded at the edges. On the top flange a wire rope was attached through a hinge formulation and properly connected to the actuator head. The test was performed with the use of a 300kN hydraulic actuator operating in displacement control. The rate control of the imposed displacement was equal to 0.032 mm/s and the reaction load was measured by a load-cell attached to the actuator. Four vertical LVDTs (V.LVDT) were installed to record the joint's extension, while two horizontal LVDTs (H.LVDT) were placed horizontally to measure any deflection of the specimen from verticality. The number of LVDTs was selected in order to increase the accuracy of the measurements and to provide sufficient amount of experimental data in order to exclude any out-of-plane movement.

Additionally, two SGs were mounted at the bottom of the specimen to record any extension of the support segment, to verify that the extension was absorbed by the joint. It is noted that preliminary numerical results of the PFJ experiment disclosed that joint's axial movement would be tensile. Thus, a tensile test was decided to be performed, rather than a compressive one.

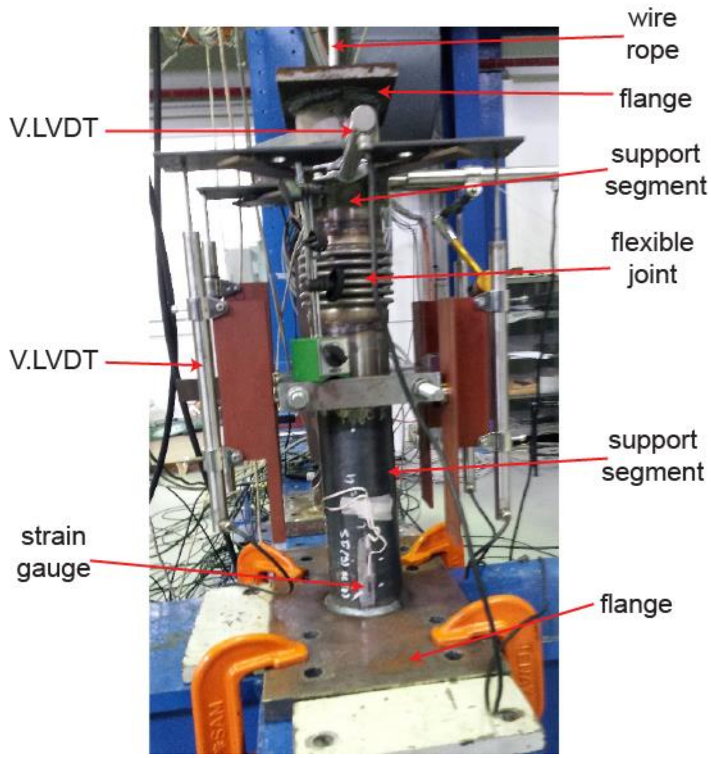

Figure 14: Joint tensile test experimental set-up and measuring devices

The experimental results are presented in terms of the equilibrium paths in Figure 15, where on the vertical axis the load monitored by the actuator's load-cell is presented and on the horizontal axis the average displacement of the four V.LVDTs. The experimental path includes also the unloading path that was not considered in processing the results. The joint behavior in tension was nearly linear until the displacement reached the value of about 72.3 mm, where the joint failed through local deformations of the convolutions (Figure 16). It is noted that local deformations were observed to develop in a quite symmetrical manner around the circumference of the joint in angles of 120 degrees. The joint's convolutions are mechanically created in a joint-forming machine through expansion of a tube. Thus, when the joint was tensioned, the convolutions were subjected to flattening that caused local deformations to form. H.LVDTs provided measurements of maximum displacement equal to 3 mm, indicating that the deviation from verticality was insignificant. The maximum tensile strain was equal to 72 μstrain, which was adequately low to assume that the imposed extension was totally absorbed by the joint.

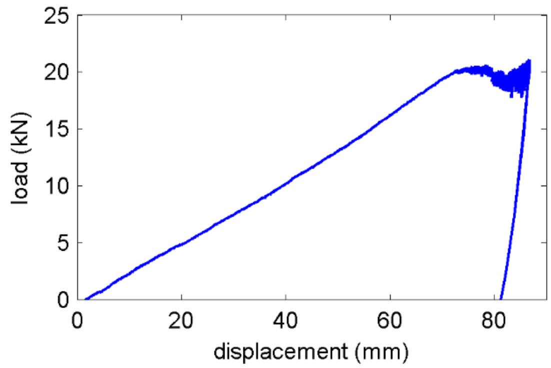

Figure 15: Experimental equilibrium path of joint tensile test

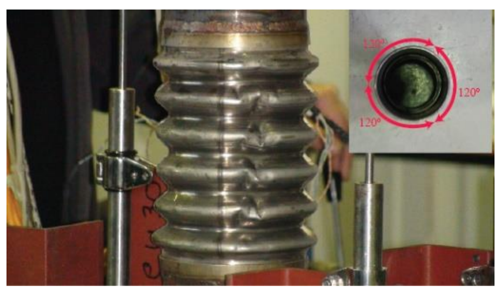

Figure 16: Joint failure in expansion through local deformations of the convolutions

A second test was performed to measure the joint angular stiffness. The experimental set-up and the measuring devices of the joint bending test are illustrated in Figure 17. The joint was welded between two CHS 114.3x3 segments; one edge was free and the other was welded to a thick steel plate, which was properly connected to a rigid base on the testing frame. The loading flange was used for this experiment and was connected to the actuator head via a wire rope through a hinge formulation, ensuring that no axial force could be imposed to the specimen and at the same time the imposed displacement would be always perpendicular to the joint undeformed axis. The test was performed using the laboratory's hydraulic actuator, operating in displacement control with rate equal to 0.032 mm/s. Two vertical LVDTs were attached through hinges on the loading flange to measure the vertical displacement. Two strain gauges were mounted at the top and bottom of the segment close to the support flange to monitor any potential bending of the supporting tube, to identify whether the imposed angular movement is fully absorbed by the joint.

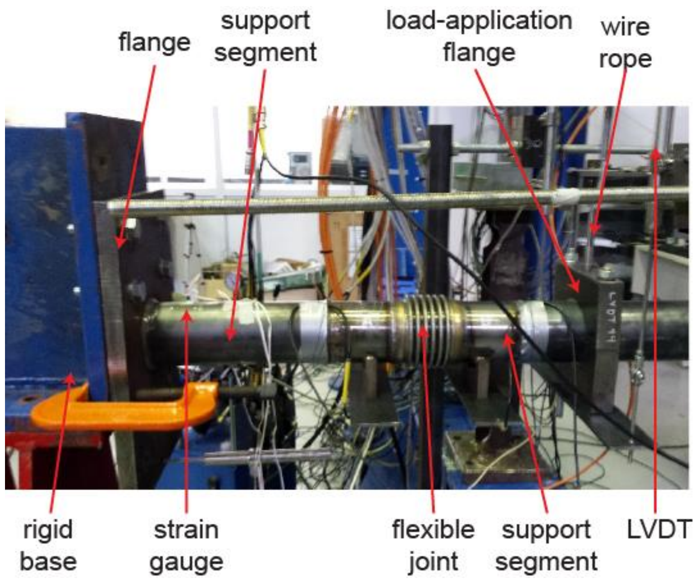

Figure 17: Joint bending test experimental set-up

The experimental results are presented in terms of the equilibrium path in Figure 18a, where the load monitored by the actuator's load-cell is presented on the vertical axis and the average displacement of the two vertical LVDTs on the horizontal axis. The joint behavior in bending is highly nonlinear. When the vertical displacement reached the value 118 mm, three convolutions got into contact and the experiment was terminated in order to protect the testing equipment and the experimental set-up from being damaged. Thus, after this point, the experimental equilibrium path in terms of load – displacement exhibits an unloading branch. At this point the joint had reached a rotation angle of over 20 degrees (Figure 19), much higher than the rotation of the joints at the test of the tube with joints, which was measured equal to 7.85 degrees. Using the geometry of the joint rotation, the force – displacement path was converted to moment – angle terms (Figure 18b). Finally, the maximum tensile strain was equal to 425 μstrain and the maximum compressive strain was 457 μstrain, indicating on the one hand that negligible axial force was imposed and on the other that strain values were sufficiently low to assume that the angular movement of the specimen was undertaken by the joint.

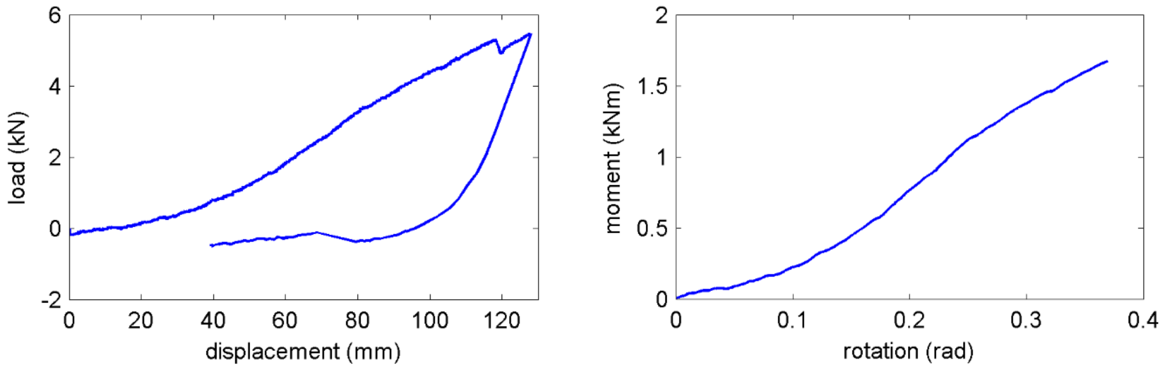

(a) (b)

Figure 18: Experimental equilibrium path of joint bending test in terms of (a) force – displacement and (b) moment – angle

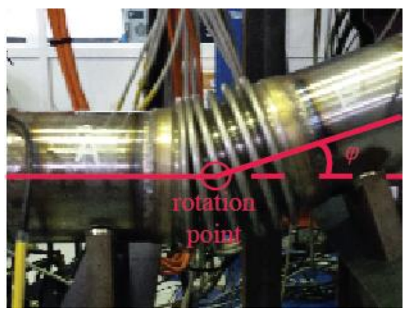

Figure 19: Nominal joint failure in bending

5. Description of numerical models and analyses

The general purpose finite element software ADINA [42] was employed for the numerical analyses. Different modeling techniques were used for the CP specimens and the PFJ specimen, based on the experimental results in terms of the developing stress-state, as will be shown later. The CP specimen was modeled both with 2-node Hermitian beam elements (FEM-beam) and with 4-node shell elements (FEM-shell), in order to identify the appropriate element. View of a CP specimen placed in the testing frame and the corresponding numerical models are shown in Figure 20. It is noted that the loading flange was not modeled, as preliminary analysis results revealed that modeling the external loading through a node connected to all nodes at the middle section of the specimen via rigid links was sufficient. The connection of the specimen to the column flange of the testing frame was represented either as rigid or through modeling of the bolted connection. The details of the connection modeling are illustrated in Figure 21. The column flange of the testing frame was meshed with shell elements and considered to be fixed. The endplate and the nuts were also meshed with shell elements. The bolts were meshed with bolt elements, which are beam-type finite elements, capable of being subjected to pretension, while they were considered to be fixed on the testing frame. Appropriate contact elements were introduced to model the contact pairs of nuts – endplate and endplate – column flange.

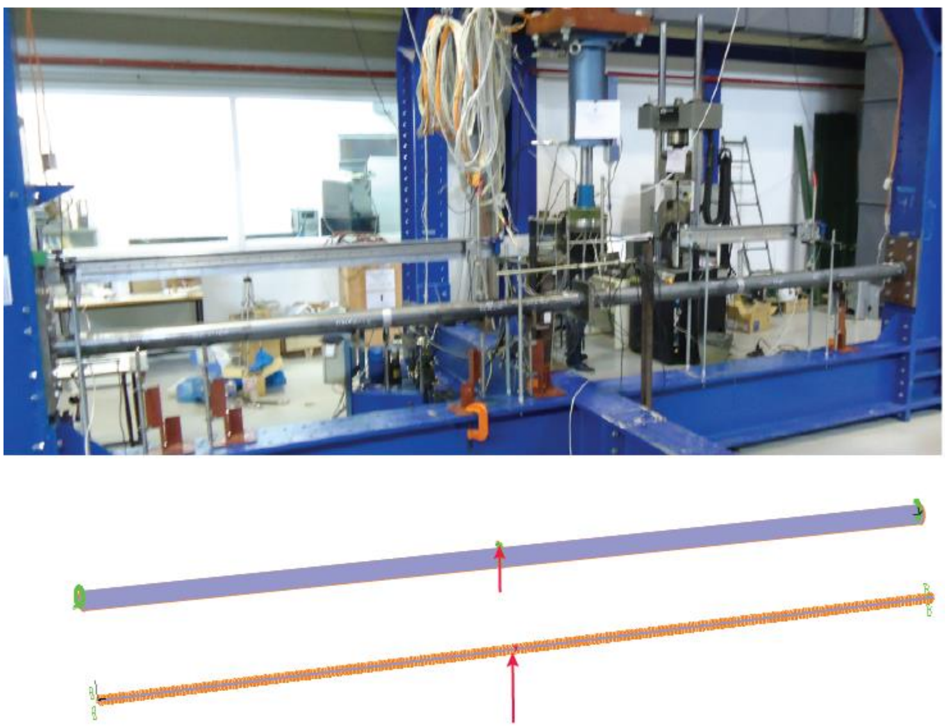

Figure 20: CP specimen at the testing frame and corresponding numerical models

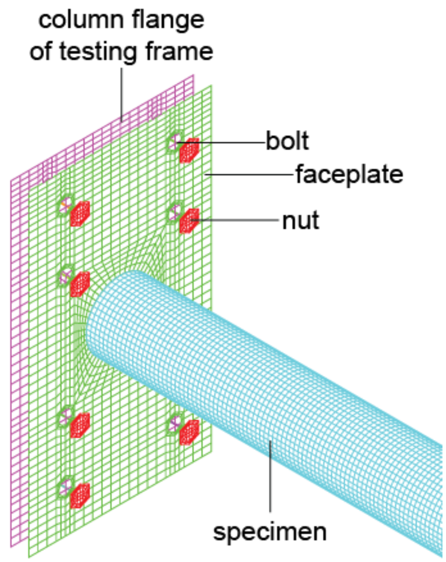

Figure 21: Modeling details of the specimen – testing frame bolted connection

The tube specimens used for the tests had been manufactured through cold-bending of steel sheets and were then seam welded. Due to this process residual stresses develop over the cross-section and along the steel member, respectively. Residual stresses are divided into: (i) circumferential stresses due to cold-bending, having nonlinear distribution through the thickness [43]. The thickness of the tube specimens was equal to 3 mm and considered to be sufficiently low so that the effect of the circumferential residual stresses could be assumed as insignificant. (ii) Longitudinal stresses due to the metallurgical alterations induced within the heat-affected zone during the seam welding procedure. Residual stresses in the tested tubes were not measured. Ross and Chen [43] carried out experimental tests and measured the longitudinal stresses due to the welding, while Gao et al. [44], presented a simplified distribution of the residual stresses distribution (Figure 22). These residual stresses were incorporated in the numerical models to qualitatively evaluate their influence. In the FEM-shell numerical approach for the CP specimens, the longitudinal residual stresses were incorporated as initial longitudinal strains, according to the material stress – strain relationship. Their modeling relied on discretizing the specimen shell into zones consisting of different element groups. Then, every element group was assigned appropriate initial strains (Figure 22). The location of the seam-weld on the cross-section defines the distribution of the residual stress. As the seam-weld of the CP specimens tested within the present study was not at the same circumferential location (Figure 23), the effect of residual stresses was different for every specimen, as will be shown later. The different element groups are illustrated in Figure 24 with different color, indicatively for specimen N=3.

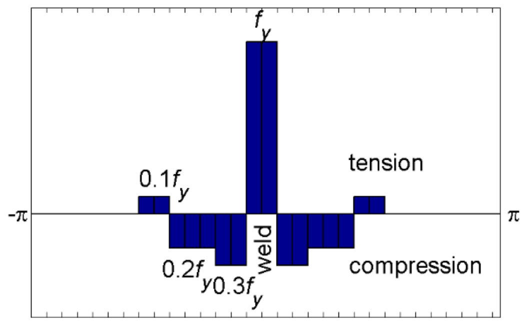

Figure 22: Longitudinal residual stresses on circular hollow section due to seam-weld [44]

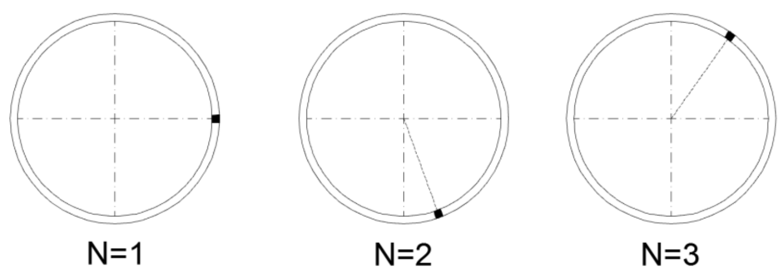

Figure 23: Seam-weld location on the cross-sectional circumference of CP specimens

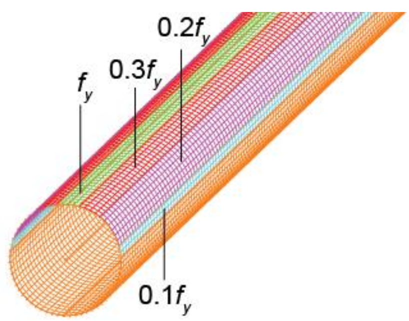

Figure 24: Modeling of longitudinal residual stresses through different element groups

The PFJ specimen was meshed into 2-node Hermitian beam-type finite elements, considering that the experimental results revealed that the specimen's behavior was entirely elastic. Flexible joints were represented by three nonlinear springs, i.e. a rotational spring to model the rotation and two translational ones to model the axial and lateral deformations [45]. Axial and angular springs' properties were obtained from the tension and bending joint tests, respectively, while the lateral spring was estimated through data sheets of joints manufacturers, as stated in section 4. This modeling technique for the bellow allowed also to indirectly incorporate the effect of residual stresses of bellows. The connections of the PFJ specimen to the testing frame were assumed to be rigid. View of the PFJ specimen placed in the testing frame and the corresponding numerical model are shown in Figure 25.

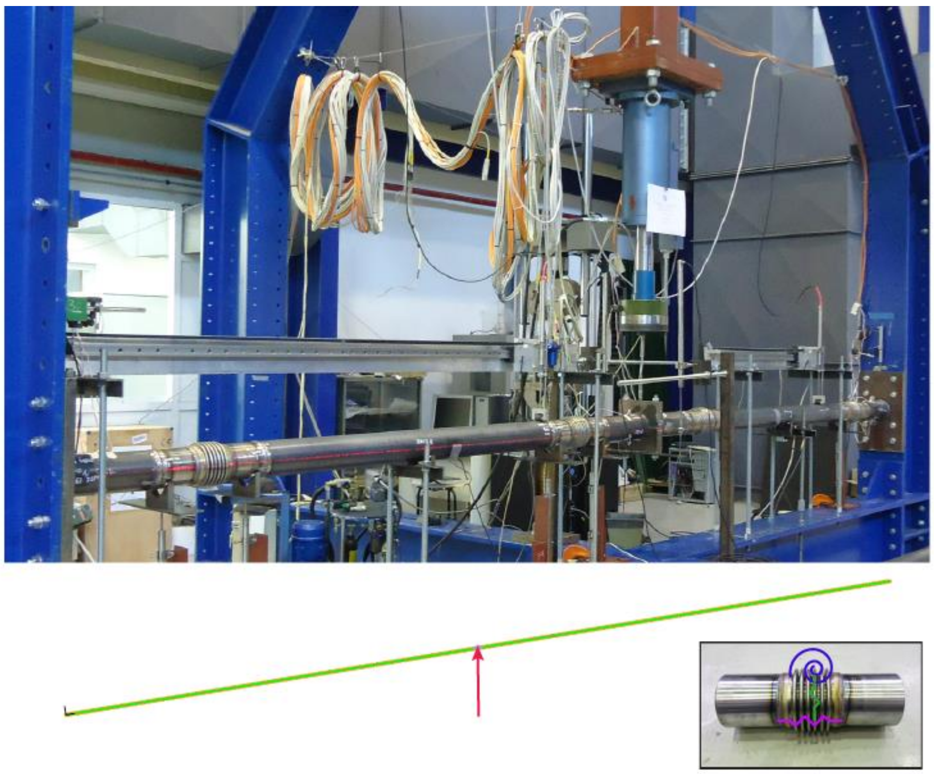

Figure 25: PFJ specimen at the testing frame and corresponding numerical model

A uniform and sufficiently dense meshing was used in all numerical models, according to the results of corresponding mesh density sensitivity analyses. The analysis was conducted in all cases in three steps: initial conditions (if applicable) were applied first, then the specimen self-weight was applied and finally, displacement was imposed. Initial conditions were different in every modeling approach. In case of detailed modeling of the specimen – testing connection, pretension of the bolts was applied in order to close any gaps between nuts – endplate and endplate – column flange, while in case residual stresses were considered, analysis was carried out to apply the initial stresses. Finally, the strategy proposed by Gantes and Fragkopoulos [46] for the numerical verification of steel structures was used in the present study. The numerical results were obtained from Geometrically and Materially Nonlinear Analyses (GMNA), in order to account for both large displacements and material yielding, using the Newton – Raphson solution algorithm and the automatic time-stepping method (ATS). ATS is used to try to obtain a converged solution by using a reduced load step during equilibrium iterations when the predetermined load steps are possibly too large. The implementation of numerical nonlinear analysis considered the practical aspects of FEM presented in [47]. It is also noted that local geometrical imperfections were not considered in the analysis, as preliminary results revealed that their effects were practically insignificant.

6. Experimental and numerical results

In this section the experimental results of continuous specimens and the specimen with flexible joints are presented and compared. Additionally, numerical results obtained from GMNAs separately for CP and PFJ specimens are presented in terms of the equilibrium paths of load – displacement, load – strain, stress and strain distributions and deformed shapes, to provide a general overview of the structural behavior.

6.1 Experimental results

6.1.1 Continuous specimens

The CP specimen deformation took place within the vertical plane defined by the specimen longitudinal axis and the imposed displacement axis. The experimental load – displacement equilibrium paths for the CP specimens are illustrated in Figure 26, where the load monitored by the actuator's load-cell is presented on the vertical axis and the average displacement obtained from the two LVDTs located on the loading flange (Figure 5) is presented on the horizontal axis. The primary observation is that the overall CP specimen behavior is nonlinear. A turning point at displacement equal to about 60 mm is detected in the equilibrium path, indicating yielding of the end cross-sections. A good match is also shown between the three specimens, indicating good repeatability of the experiment.

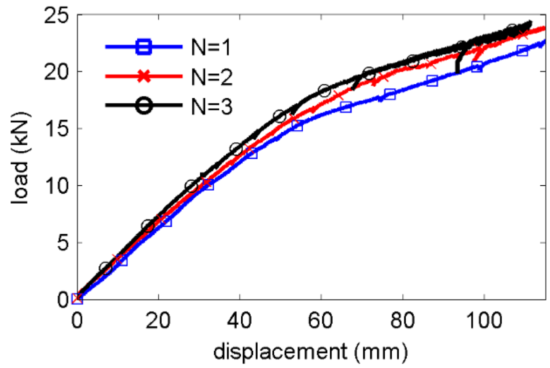

Figure 26: Load – displacement experimental equilibrium paths of CP specimens

Further comprehension of the CP specimen's behavior can be provided by comparing the experimental equilibrium paths to a simplified analytical one, considering concentrated plastic hinge formulation. The specimen steel stress – strain relationship is considered as elastic – plastic without hardening. The equivalent analytical static model in the elastic range is that of a beam with fixed ends subjected to concentrating loading *P* in the middle-span. In such case the maximum moment is developed at the fixed ends and at the middle, where the loading is applied. After the formation of the plastic hinges, it is assumed that additional imposed displacements are resisted through developing tension. The analytical load – displacement equilibrium path is compared to the experimental ones in Figure 27, where the reaction load is presented on the vertical axis and the middle-span deflection on the horizontal axis. A sufficient match is shown regarding the elastic and the post-yielding tube behavior, apart from the transition area, where premature yielding of the specimens is evident.

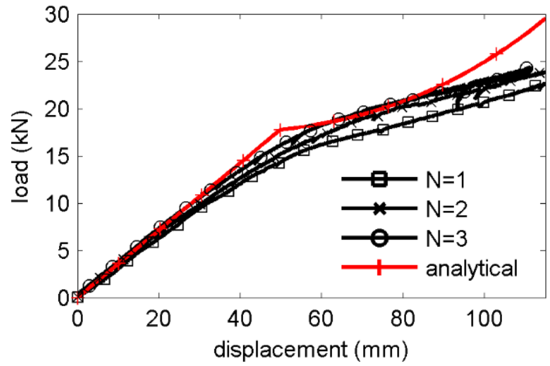

Figure 27: Experimental and analytical equilibrium paths of CP specimens

Furthermore, yielding of the end cross-sections was verified via the strains recorded by the strain gauges. Specifically, the tensile strains from SG-A1 and SG-B2 are presented in Figure 28a and Figure 28b, respectively. It is observed that strain measurements from CP specimens were in practice identical within the elastic range of the tube behavior until yielding took place for displacement equal to around 60 mm. Then, a turning point in the strain – displacement curves was detected and thereafter minor differences were reported on the tensile and the compressive strains. The strain variations after yielding were attributed to the sensitivity of the strain gauges in the post-yielding area in combination with the redistribution of strains within the cross-section due to the gradual formation of the plastic hinge.

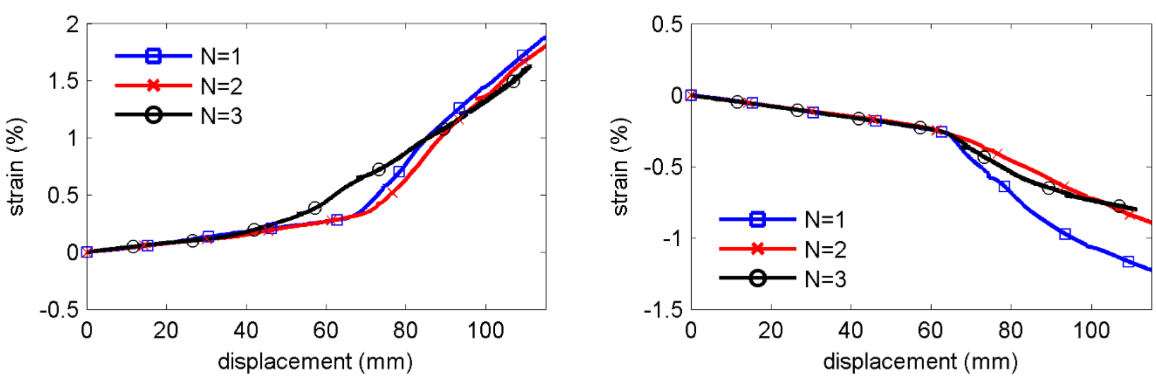

(a) (b)

Figure 28: Strains of CP specimens: (a) tensile from SG-A1 and (b) compressive from SG-B2

6.1.2 Specimen with flexible joints

The experimental load – displacement equilibrium path of PFJ specimen is depicted in Figure 29, where the load monitored by the actuator's load-cell is presented on the vertical axis and the average displacement obtained from the two LVDTs located on the loading flange (Figure 5) is presented on the horizontal axis. The major observation is that load values were almost two orders of magnitude smaller than for the CP specimens and that there was not a clearly visible equilibrium path, but instead a cloud of measurements was recorded due to the sensitivity of the load-cell that was not fully capable of monitoring such low load values. Additionally, load measurements from the onset of the test were above zero, as the actuator was loaded approximately with half of the specimens' self-weight, due to the inability of the joints to provide appreciable flexural resistance. Then, similarly to the load – displacement cloud, the tensile strain cloud recorded from SG-A1 (Figure 5) and the compressive strain cloud from SG-B2 (Figure 5) are shown in Figure 30a and Figure 30b, respectively. The strain equilibrium paths are ascending, indicating the increase of the developing stress-state with reference to the displacement. Most importantly, strains are three orders of magnitude smaller than for the CP specimens, confirming the efficiency of flexible joints in protecting the tube from strain-related failure modes, such as local buckling and tensile fracture, as outlined in more detail in the following section. It is noted that experimentally obtained forces and strains of PFJ specimen were in practice negligibly small and actual values did not matter. Finally, it has to be noted that the developed deformations of the bellows at the end of the experiment were sufficiently lower than the ultimate values estimated from the individual experiments of the bellows. In practical applications of bellows in buried pipes, bellows with sufficient deformation capacity must be specified, so that they can elastically absorb the anticipated deformations in case of fault activation.

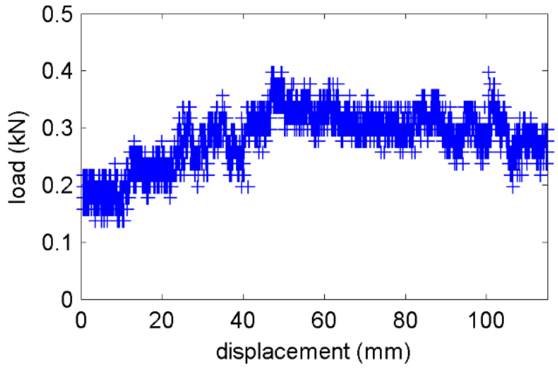

Figure 29: Load – displacement experimental equilibrium paths of PFJ specimen

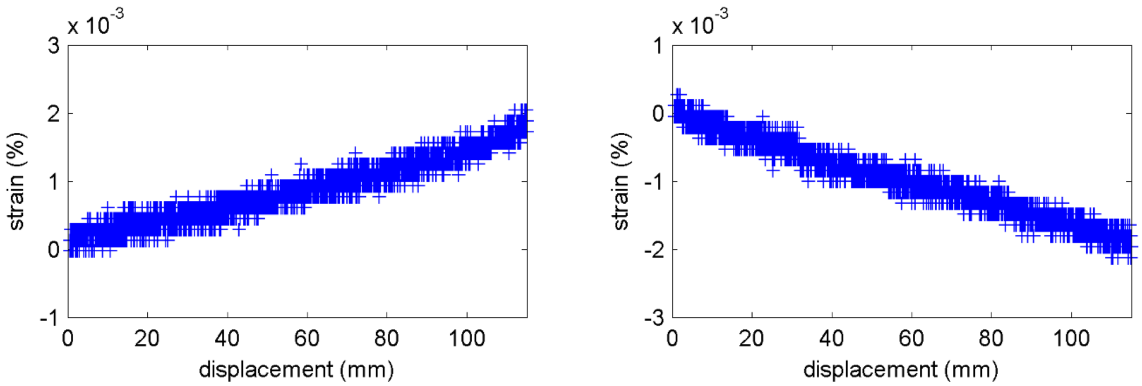

(a) (b)

Figure 30: Strains of PFJ specimen: (a) tensile from SG-A1 and (b) compressive from SG-B2

6.1.3 Comparison of experimental results

The comparison of CP and PFJ specimens' results is crucial to identify and quantify the effect of flexible joints in terms of strain reduction considering that the pipeline design against faulting is strain-based. Results presented in sections 6.1.1 and 6.1.2 for CP and PFJ specimens, respectively, indicate that the introduction of joints has led to a significant decrease of load and developing tensile and compressive strains. Thus, the primary research objective of the present experimental study has been highlighted, namely, the considerable contribution of flexible joints in strain reduction in the pipe parts of the tested specimen has been confirmed. This provides optimistic indications that flexible joints have the potential to be an effective mitigating measure for the protection of buried pipelines subjected to faulting, provided that the issues identified in section

1 have been addressed and resolved. It is noted that the significant differences regarding strain and force development in CP and PFJ specimens that was reported state that the graphical comparison of results through load – displacement and strain – displacement curves could not be viable. Therefore, a tabular comparison is presented by listing the maximum developed load and strains in Table 3, where strain gauge numbering refers to Figure 5. It is observed that PFJ load and strains were two and three orders of magnitude lower, respectively, compared to CP specimens. The significant differences regarding the maximum values of strains obtained from the ~~three~~ CP specimens are due to the local redistribution of strains caused by cross-section yielding, so that maximum strain values do not, in general, occur at the locations of strain gauges.

Table 3: Comparison of CP and PFJ experimental results in terms of maximum load and strains

specimen	load (kN)	max compressive strain SG-B2 (%)	max tensile strain SG-A1 (%)	max tensile strain SG-A4 (%)	max compressive strain SG-A3 (%)
N=1 (CP)	24.61	-1.25	2.24	1.91	-1.08
N=2 (CP)	23.56	-0.79	1.81	1.42	-0.51
N=3 (CP)	23.79	-0.37	1.63	1.55	-0.89
N=4 (PFJ)	0.30	-0.0016	0.0017	0.0015	-0.0017

6.2 Experimental and numerical results

The experimental results are compared with numerical ones separately for CP and PFJ specimens in this section. CP results showed that yielding took place at the critical cross-sections, namely the fixed ends and the middle. On the other hand, experimental PFJ results revealed that its behavior was fully elastic.

6.2.1 Continuous specimens

The experimental equilibrium paths are compared to the numerical ones. Initially, two investigations were carried out, namely specimen meshing with either beam- or shell-type finite elements and boundary conditions modeled either as rigid or as semi-rigid, by detailed modeling of the bolted connection, in order to confirm that the connection is sufficiently stiff and does not affect the specimen's response. The comparison of equilibrium paths regarding the type of finite elements by considering rigid boundary conditions is shown in Figure 31, where the experimental paths of CP specimens (test) are examined in contrast with the numerical paths (FEM-beam and FEM-shell). The vertical displacement of the loading flange is presented on the horizontal axis and the load on the vertical one. The FEM modeling approach appeared to have a small effect on the post-yielding branch, while the elastic branches practically coincide.

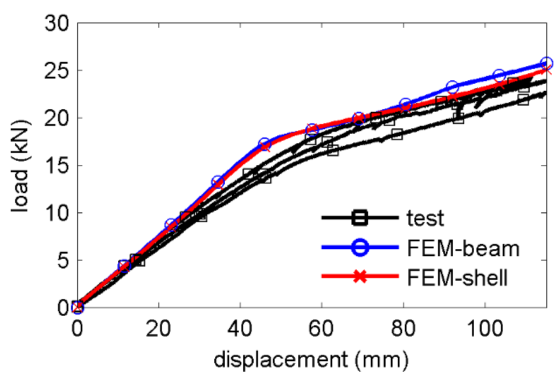

Figure 31: Experimental and numerical equilibrium paths of CP specimens considering the finite element type

Secondly, the effect of boundary conditions was addressed and the equilibrium paths are illustrated in Figure 32, where the CP experimental results (test) are compared to the numerical ones employing shell elements and considering either rigid end conditions (FEM-fixed) or connection modeling (FEM-connection). The major finding was that the boundary conditions did not modify the response of the numerical models, as the corresponding paths practically coincide. Therefore, modeling the boundary conditions as rigid was proven to be sufficient.

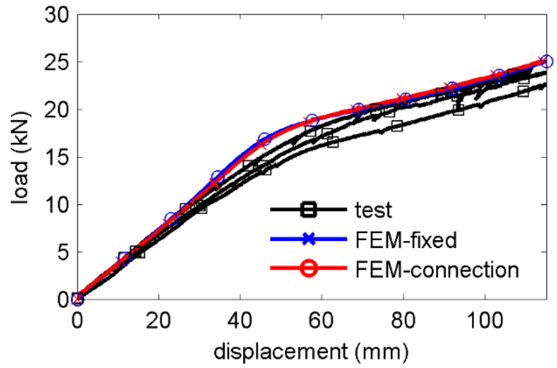

Figure 32: Experimental and numerical equilibrium paths of CP specimens considering the numerical boundary conditions

However, numerically obtained equilibrium paths demonstrated that the model was not fully capable of capturing the gradual and premature yielding exhibited by the experimental specimens. In order to investigate whether this can be attributed to the presence of longitudinal residual stresses caused by the seam-weld, such stresses were incorporated in the model, through the process described in section 5, in order to account for the material alternations caused by the welding in the heat affected zone. The location of the seam weld on the tube circumference was different in every specimen (Figure 23). Experimental (test) and numerical equilibrium paths in terms of load – displacement (FEM-residual) are presented in Figure 33, while for comparison reasons the numerical equilibrium path without considering residual stresses (FEM-no-residual) is also depicted.

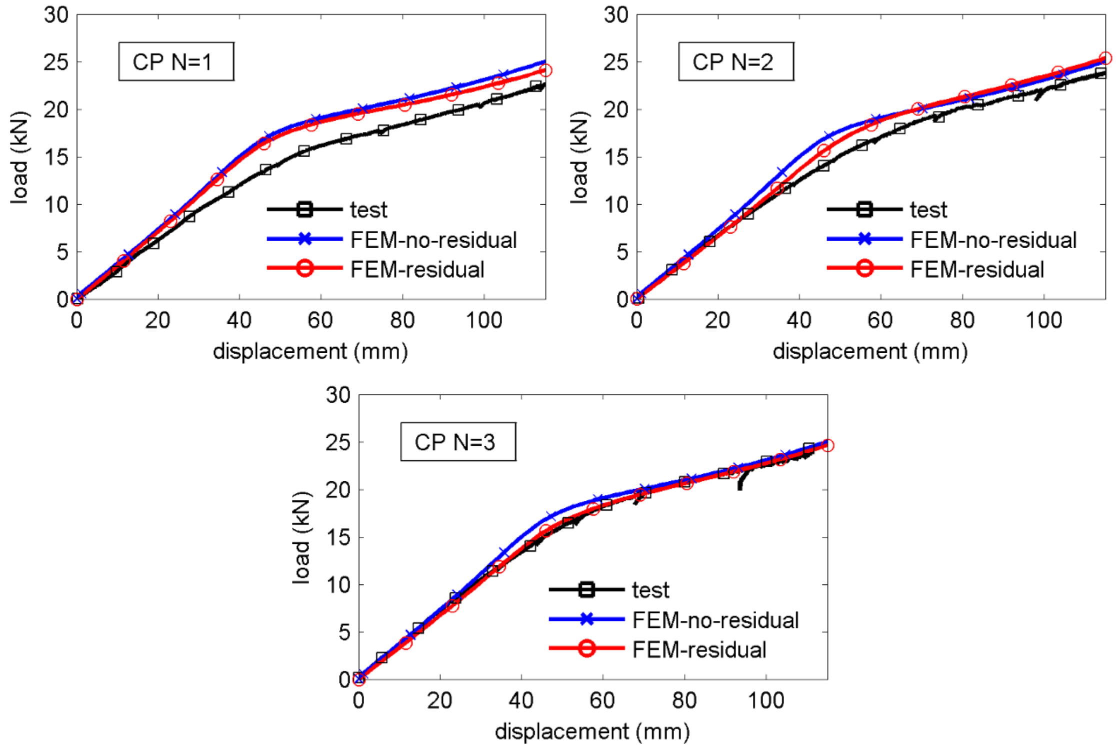

Figure 33: Comparison of experimental and numerical load – displacement equilibrium paths of CP specimens by considering longitudinal residual stresses

It can be seen that the incorporation of residual stresses did not substantially improve the agreement between the numerical and the experimental results in all specimens, due to the different location of the seam weld with respect to the neutral axis. As shown in Figure 22, steel is subjected to tension in the vicinity of the weld due to the heat treatment of the material caused by the welding procedure. Then, along the circumference of the cross-section the subsequent area is compressed to balance the above tension. Similarly, the final narrow affected zones are tensioned. This sequence of residual tension and compression around the seam-weld heavily affects the material behavior, while it expands over half of the cross-section. Based on the aforementioned "analysis", the results of Figure 33 can be evaluated. The seam weld in specimen N=1 was located in the region of the cross-section neutral axis and therefore the weld heat affected zone did not extend over the cross-section areas where maximum tension and compression developed at the critical cross-sections. Hence, considering the longitudinal residual stress did not significantly improve the numerical results. Then, in specimen N=2, the seam weld was located near the area, where the maximum tension was developed at the critical sections (specimen – endplate connection). Therefore, the effect of residual tension and compression was more significant than in specimen N=1, which was verified by the fact that the “FEM-residual” model captured the tube yielding more accurately than the “FEM-no-residual” one. Finally, in specimen N=3 the match between the numerical and the experimental results was concluded to be significantly good due to the location of the seam weld near the maximum developed compression at the critical cross-sections. In practice, the area where compression developed due to external loading was already compressed by the residual stresses and consequently yielding took place for lower displacement level than without accounting for residual stresses. Remaining differences between experimental and numerical equilibrium paths were attributed to small deviations of specimens from straightness.

The numerical predictions of the specimens’ deformation at various levels of imposed displacement are presented in Figure 34 indicatively for specimen N=1, where the longitudinal specimen axis is presented on the horizontal axis and the specimen vertical displacement, as defined by the external loading direction, on the vertical axis. The numerically obtained specimen’s deformation is abbreviated as FEM, the LVDT measurements as test-LVDT and the one recorded by the deformation plotter as test-DP. Similar results were extracted for specimens N=2 and N=3.

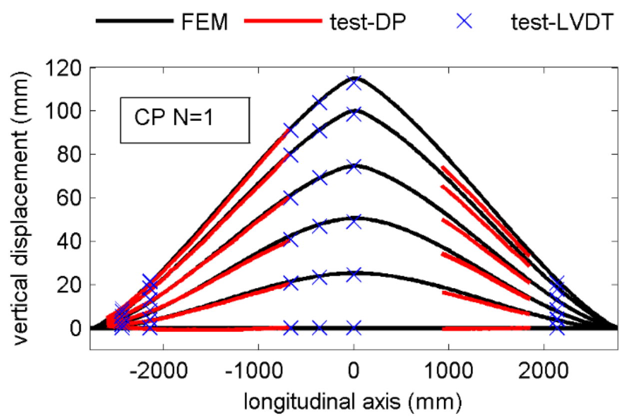

Figure 34: Experimental and numerical deformation of CP specimen N=1 at various levels of imposed displacement

Finally, numerical strain predictions are presented in Figure 35 in terms of strain – displacement curves of CP specimens, where the tensile (Figure 35a) and the compressive (Figure 35b) strains of the critical cross-sections (boundary sections where the maximum stress-state is developed) are presented on the vertical axis, while the vertical displacement of the specimen's middle on the horizontal axis. The comparison of numerically and experimentally obtained strains revealed that there was a sufficiently good match in the elastic range. However, numerical models showed steel yielding taking place for higher displacement than experimental results and consequently numerically extracted strains were higher than the experimental ones, which was attributed to the sensitivity of strain measurement in the plastic range. Finally, the elastic and plastic regions, as predicted numerically, are shown in Figure 36. The fact that the tensile plastic zones are more extended than the compressive ones indicates that the specimen develops a tensile axial force after formation of plastic hinges.

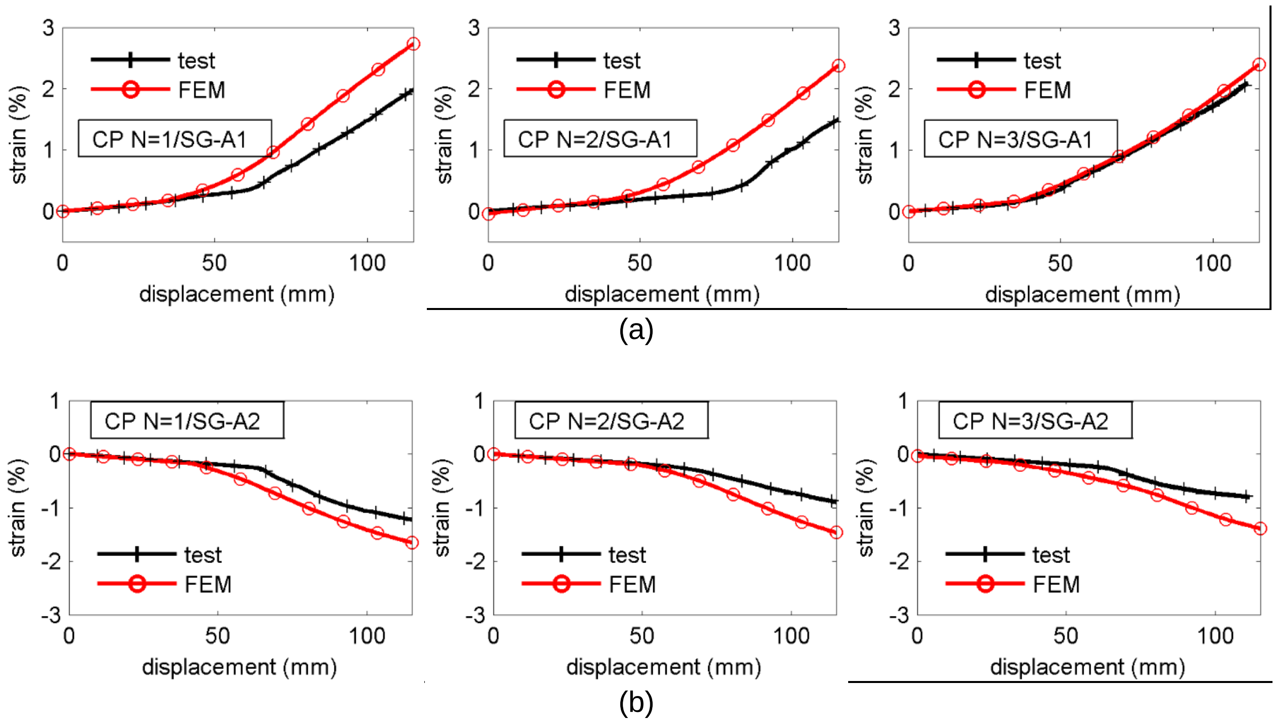

Figure 35: Experimental and numerical strain – displacement curves of CP specimens: (a) tensile strains and (b) compressive strains at critical sections (maximum developed stress-state)

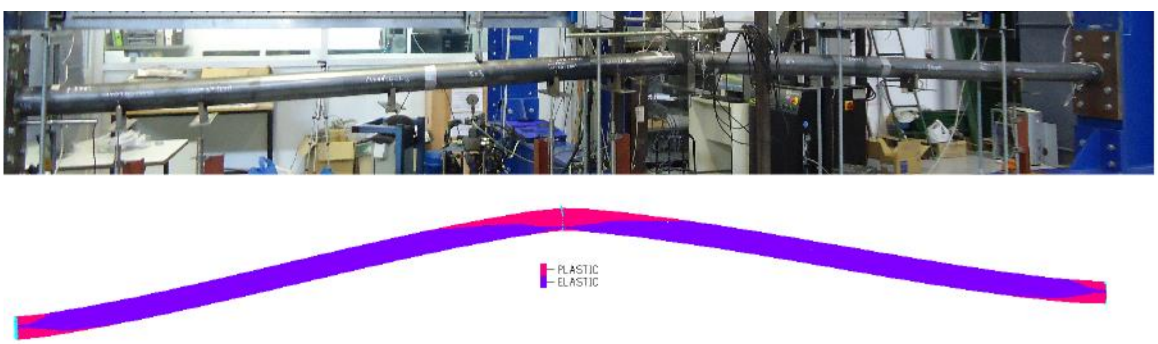

Figure 36: Elastic and plastic regions of failure of CP specimen N=1

6.2.1 Specimen with flexible joints

The specimen with flexible joints was modeled with beam-type finite elements, as presented in section 5 and the boundary conditions were assumed to be rigid. This modeling approach was selected based on the corresponding experimental results, which showed that the developed stress-state was very low, compared to CP specimens and at the same time experimental recordings were within the range of sensitivity of the measuring devices. The experimental equilibrium path is compared to the numerical one in Figure 37a, where the displacement of the loading flange is presented on the horizontal axis and the load on the vertical axis. The numerical path was shown to exhibit different stiffening behavior, indicating cable-type of action, due to the negligible flexural stiffness of the tube with internal flexible joints. The specimen self-weight was considered in the numerical analysis and thus the load – displacement path's onset was equal to about half the self-weight, while due to the limiting sensitivity of the load-cell for such low recordings, the onset of the experimental path is quite lower. However, considering the aforementioned limitations of the experimental monitoring process, the numerical model prediction of the specimen behavior is satisfactory. It is noted that regarding the joint lateral stiffness, where no experiment was carried out, parametric analyses conducted with reference to the axial stiffness obtained from manufacturers' data revealed that its role to the specimen's behavior was very limited. It was thus decided to adopt an axial over lateral joint stiffness ratio equal to 0.50. Finally, experimental and numerical specimen's deformed shape at various levels of the imposed displacement by the actuator is illustrated in Figure 37b, where the vertical specimen displacement (in-line with loading application) is plotted on the vertical axis, while the specimen's longitudinal axis is plotted on the horizontal axis. The numerically obtained deformed shape is presented as FEM, while the experimental results are represented by the measurements of the individual LVDTs (test-LVDT) and the Deformation Plotters (test-DP). The major finding is that results showed a comprehensive match and the assumed numerical approach is sufficient to model the behavior of the specimen with flexible joints. This numerical modeling approach was adopted in [40] to conduct extensive parametric studies in order to investigate the parameters affecting the behavior of buried pipes with flexible joints, such as pipe – fault crossing angle, burial depth and fault trace uncertainty, proposing also rules for joint placement along the pipeline.

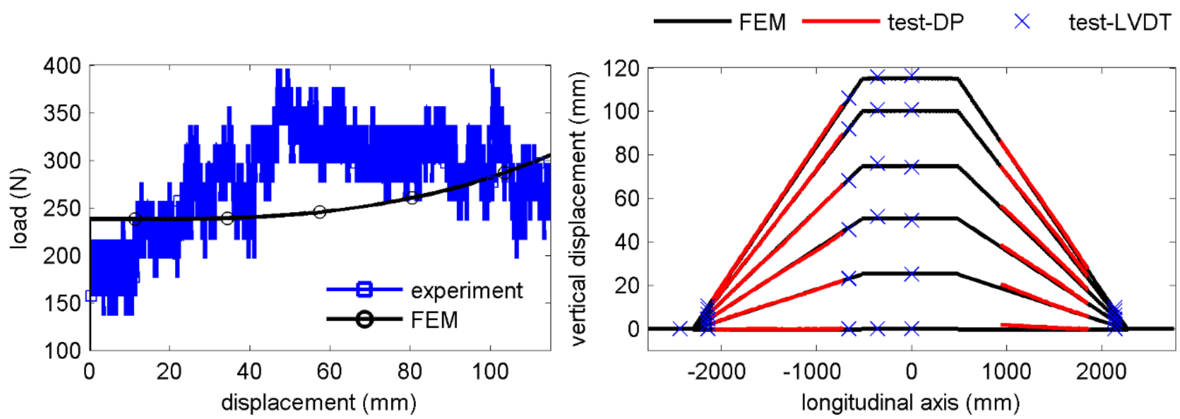

(a) (b)

Figure 37: Summary of experimental and numerical results for PFJ specimen including (a) load – displacement equilibrium path, (b) experimental and numerical specimen deformation at various levels of imposed displacement

As a final remark, the transformation of the continuous structural system of the tube to segmented due to the integration of flexible joints can be clearly seen in Figure 38, where the CP N=1 and PFJ N=4 specimen's final deformed shapes are presented.

(a)

(b)

Figure 38: Comparison of (a) CP and (b) PFJ specimen's experimental deformations at the test end

6. Summary and conclusions

The results of experimental tests and corresponding numerical simulations of continuous tubes and a tube with flexible joints under imposed transverse displacement, modeling the deformation of a pipe subjected to strike-slip fault rupture, have been presented. The purpose of integrating bellow-type flexible joints in a continuous tube, is to transform the structural system from continuous to segmented, and consequently to absorb the deformations due to imposed transverse displacements by joint rotations, thus preventing failure of the steel parts. Objective of this investigation was to demonstrate the efficiency of this concept and to calibrate numerical models for subsequent numerical parametric studies. These goals have been achieved in a satisfactory manner.

Namely, maximum compressive and tensile strains, which are a measure of the pipe's susceptibility to failure by local buckling and girth weld fracture, respectively, have been reduced by three orders of magnitude due to the integration of bellow-type flexible joints, practically eliminating the risk of these two failure modes. In addition, satisfactory prediction of test results by numerical analyses was possible, modeling the pipe segments with beam elements and the joints with equivalent springs.

The presented investigation is part of a feasibility study on the use of bellows along pipes crossing active faults. The results have provided confidence on the effectiveness of such joints in reducing the developing longitudinal strains of the pipe, highlighting them as a promising protective measure in such cases. In practical applications bellows with sufficient deformation capacity must be specified, so that they can accommodate imposed deformations behaving elastically. Moreover, several constructional considerations must be resolved before this concept can be actually implemented, such as bellow protection against corrosion, pipe – bellow proper welding and bellow long-term behavior.

AKNOWLEDGMENTS

This research has been co-financed by the European Union (European Social Fund – ESF) and Hellenic National Funds through the Operational Program “Education and Lifelong Learning” (NSRF 2007-2013) – Research Funding Program “Aristeia II”, project “ENSSTRAM - Novel Design Concepts for Energy Related Steel Structures using Advanced Materials”, grant number 4916. The authors would like to express their gratitude to Dr. Dimitrios Lignos, Professor at the Ecolé Polytechnique Fédérale de Lausanne for his help in validating the numerical models vs experimental results and to Mr. S. Katsatsidis of the Institute of Steel Structures of the School of Civil Engineering at the National Technical University of Athens for his invaluable help in performing the tests.

REFERENCES

[1] O’Rourke MJ, Liu X. Seismic design of buried and offshore pipelines. Monograph No. 4”. Buffalo: Multidisciplinary Center for Earthquake Engineering Research; 2012.

[2] Gantes CJ, Bouckovalas GD. Seismic verification of high pressure natural gas pipeline Komotini – Alexandropoulis – Kipi in areas of active fault crossings. Struct Eng Int 2013;2:204-8. DOI: 10.2749/101686613X13439149157164

[3]Bekki H, Kobayashi K, Tanaka Y, Asada T. Dynamic behavior of buried pipe with flexible joints in liquefied ground. J Japan Sewage Assoc 2002;39:201-8.

[4] Melissianos VE, Vamvatsikos D, Gantes CJ. Probabilistic assessment of innovative mitigating measures for buried steel pipeline – fault crossing. In: Proceedings of the ASME 2015 Pressure Vessels & Piping Conference; 2015 Jul 19-23; Boston, Massachusetts, USA.

[5] Murphey CE. Ultimate pipe strength under bending, collapse and fatigue. Shell Development Company, Pipeline R & D Laboratory, Deepwater Pipeline Feasibility Study, Section 21-1, Houston, 1975.

[6] Reddy BD. An experimental study of the plastic buckling of circular cylinders in pure bending. Int J. Solids Structures 1979;15:669-83.

[7] Korol RM. Critical buckling strains of round tubes in flexure. Int. J. Mech. Sci. 1979;21:719-30.

[8] Kimura TS, Idogaki K, Takada K, Fujita Y. Experimental and analytical studies of the elasto-plastic behavior of offshore pipelines during laying. In: Offshore Technology Conference, paper 3737; 1980, Houston, USA.

[9] Gresnigt AM. Plastic design of buried steel pipelines in settlement areas. HERON, Vol. 31, No. 4, 1986.

[10] Yoosed-Ghodsi N, Kulak GL, Murray DW. Some test results for wrinkling of girth welded line pipe. In: Proceedings of the 14th International Conference on Offshore Mechanics and Arctic Engineering (OMAE), Vol. V – Pipeline Technology, pp. 379-388; 1995 Jun 18-22; Copenhagen, Denmark.

[11] Murray DW. Local buckling, strain localization, wrinkling and postbuckling response of line pipe. Eng Struct 1997;19(5):360-71. DOI: 10.1016/S0141-0296(96)00096-X

[12] Gresnigt AM, van Foeken RJ, Chen SL. Collapse of UOE manufactured steel pipes. In: Proceedings of the Tenth International Offshore and Polar Engineering Conference (ISOPE), Vol. II, pp. 170-181; 2000 May 28 – June 2; Seattle, USA.

[13] Gresnigt AM, van Foeken RJ. Local buckling of UOE and Seamless Steel Pipes. In: Proceedings of the Eleventh (2001) International Offshore and Polar Engineering Conference, 2001 Jun 17-22, Stavanger, Norway.

[14] Dama E, Karamanos SA, Gresnigt AM. Failure of locally buckled pipelines. J Pres Vessel Techn 2007;29(2):272-9. DOI: 10.1115/1.2716431

[15] Thinvongpituk C, Poonaya S, Choksawadee S, Lee M. The ovalization of thin-walled circular tubes subjected to bending. In: Proceedings of the World Congress on Engineering Vol II; 2008 Jul 2-4; London, UK.

[16] Gresnigt AM, Karamanos SA. Local buckling strength and deformation capacity of pipes. In: Proceedings of the Nineteenth (2009) International Offshore and Polar Engineering Conference; 2009 Jun 21-26; Osaka, Japan.

[17] Mason JA, O'Rourke TD, Jung JK. Direct tension performance of steel pipelines with welded slip joints. ASCE J Pipeline Syst Eng Pract 2010;1(4):133-40. DOI: 10.1061/(ASCE)PS.1949-1204.0000063

[18] Chen H, Ji L, Huang C, Wang H, Li Y. Analysis of bending test of 40-in X70 line pipe. In: Proceedings of the Twenty-second (2012) International Offshore and Polar Engineering Conference; 2012 Jun 17-23; Rhodes, Greece.

[19] Ferino J, Fonzo A, Porta R, Spinelli CM. Analytical formulation for line pipe bending strain capacity evaluation developed through experimental – numerical approach. In: Proceedings of the Twenty-third (2013) International Offshore and Polar Engineering Conference; 2013 Jun 30 – Jul 5; Anchorage, Alaska, USA.

[20] Kristoffersen M, Borvik T, Langseth M, Hopperstad OS. X65 steel pipes subjected to combined stretching and bending. In: Proceedings of the VI International Conference on Computational Methods in Marine Engineering; 2015 Jun 15-17; Rome, Italy.

[21] American Petroleum Institute. Specification for line pipe, 44th ed. ANSI/API Spec 5L, 2007.

[22] American Society of Mechanical Engineers. Pipeline transportation systems fdor liquid hydrocarbons and other liquids. ANSI/ASME 2006;B31:4.

[23] American Society of Mechanical Engineers. Gas transmission and distribution piping systems. ANSI/ASME 2007;B31:8/

[24] Z245.1-95. Steel line pipe, Oil & Gas industry systems and materials, Canadian Standards Association, 1995, Etobicoke, Ontario, Canada.

[25] Z662-96. Oil and gas pipeline systems, Canadian Standards Association, 1996, Etobicoke, Ontario, Canada.

[26] DNV-OS-F101.Offshore Standard OF-F101, Submarine pipeline systems, Det Norske Veritas, Hovik, Norway.

[27] Abdoun TH, Ha D, O'Rourke MJ, Symans MD, O'Rourke TD, Palmer MC, Stewart HE. Factors influencing the behavior of buried pipelines subjected to earthquake faulting. Soil Dyn Earth Eng 2009;29(3):415-27. DOI: 10.1016/j.soildyn.2008.04.006

[28] Ha D, AbdounTH, O'Rourke MJ, Symans MD, O'Rourke TD, Palmer MC, Stewart HE. Earthquake faulting effects on buried pipelines – case history and centrifuge study. J Earth Eng 2010;14(5):646-669. DOI: 10.1080/13632460903527955

[29] Earthquake Engineering Research Institute. Kocaeli, Turkey Earthquake of August 17. Pasadena: EERI; 1999.

[30] Rofooei FR, Jalali HH, Attari NKA, Alavi M. Full-scale laboratory testing of buried pipelines subjected to permanent ground displacement caused by reverse faulting. In: Proceedings of the 15th World Conference on Earthquake Engineering; 2012 Sept 24-28; Lisbon, Portugal.

[31] Moradi M, Rojhan M, Galandarzadeh A, Takada S. Centrifuge modeling of buried continuous pipelines subjected to normal faulting. J Earth Eng and Eng Vibr 2013;12(1):155-64. DOI: 10.1007/s11803-013-0159-z

[32] RFCS, Safety of buried steel pipelines under ground-induced deformations. Final report of GIPIPE project, EU Directorate-General for Research and Innovation, Luxemburg; 2015. DOI:10.2777/9147

[33] Hedge AM, Sitharam TG. Experimental and numerical studies on protection of buried pipelines and underground utilities using geocells. Geotextiles and Geomembranes 2015;43:372-81. DOI: 10.1016/j.geotexmem.2015.04.010

[34] Sim WW, Towhata I, Yamada S, Moinet GJ-M. Shaking table tests modelling small diameter pipes crossing a vertical fault. Soil Dyn Earthq Eng 2012;35:59-71. DOI: 10.1016/j.soildyn.2011.11.005

[35] Monroy-Concha M. Soil restraints on steel buried pipelines crossing active seismic faults [dissertation]. Canada: The University of British Columbia; 2013.

[36] Medeiros J, Veiga JLB, Veiga JCC. Analysis of FCC expansion joints movement test. In: Proceedings of the ASME 2009 Pressure Vessels and Pipeline Division Conference; 2009 Jul 26-30; Prague, Czech Republic. DOI: 10.1115/1.4027201

[37] Veiga JC, Kavanagh N, Sousa AMF, Medeiros J, Veiga JL. Determination of gimbal and hinged expansion joints reaction moments. ASME J Pressure Vessel Technology 2013;135:055001. DOI: 10.1115/1.4024435

[38] ALA American Lifelines Alliance. Guideline for the design of buried steel pipe – July 2001 (with addenda through February 2005). American Society of Civil Engineers, New York, USA; 2005.

[39] Comité Européen de Normalisation. Eurocode 8, Part 4: Silos, tanks and pipelines. CEN EN 1998-4, Brussels, Belgium; 2006.

[40] Melissianos VE, Korakitis GP, Gantes CJ, Bouckovalas GD. Numerical evaluation of the effectiveness of flexible joints in buried pipelines subjected to strike-slip fault rupture. Soil Dyn Earth Eng 2016;90:395-410. http://dx.doi.org/10.1016/j.soildyn.2016.09.012

[41] EN ISO 6892-1:2009. Metallic materials – Tensile testing – Part 1: Method of test at room temperature. March 2009.

[42] ADINA R & D Inc. Theory and Modeling guide Volume I: ADINA, Report AED 06-7, Watertown; 2006.

[43] Ross DA, Chen WF. Tests of fabricated tubular columns. In: Proceedings of the ASCE National Water Resources Conference; 1976, paper 447.

[44] Gao S, Usami T, Ge H. Ductility of steel short cylinders in compression and bending. ASCE J Eng Mech 1998;124(2):176-83. DOI: 10.1061/(ASCE)0733-9399

[45] Peng LC, Peng A. Pipe stress engineering, New York: ASME Press; 2009.

[46] Gantes CJ, Fragkopoulos E. Strategy for numerical verification of steel structures at the ultimate limit state. Struct Infrastruct Eng 2010;6:225-55. DOI: 10.1080/15732470802664449

[47] Kojic M, Bathe KJ. Inelastic analysis of solid and structures, Computational fluid and solid mechanics series, Berlin: Springer Verlag; 2004.